Acta Materialia 135 (2017) 14–24

Contents lists available at ScienceDirect

Acta Materialia

journal homepage: www.elsevier.com/locate/actamat

Full length article

Individual effect of recrystallisation nucleation sites on texture weakening in a magnesium alloy: Part 1- double twins

Dikai Guan, W. Mark Rainforth*, Junheng Gao, Joanne Sharp, Brad Wynne, Le Ma

Department of Materials Science and Engineering, University of Sheffield, Sheffield, S1 3JD, UK

ARTICLE INFO

Article history:
Received 11 March 2017
Received in revised form
1 June 2017
Accepted 7 June 2017
Available online 8 June 2017

Keywords:
Magnesium alloy
Recrystallisation
Deformation twin
Texture evolution
Precipitation

ABSTRACT

Recrystallised grain nucleation, grain growth and corresponding texture evolution in a cold-rolled rare earth containing WE43 Mg alloy during annealing at 490 °C was fully tracked using a *quasi-in-situ* electron backscatter diffraction method. The results show nucleation sites, such as double twins, can weaken the deformed texture and for the first time provide direct evidence that recrystallised grains originating from double twins can form the rare earth texture during annealing. Precipitation and recrystallisation occurred concurrently during most of the annealing period, with precipitates forming preferentially along prior grain and twin boundaries. These precipitates effectively retard the recrystallisation due to particle pinning leading to an excessively long time for the completion of recrystallisation. A large portion of recrystallised grains were observed to have ⟨0001⟩ poles tilted 20–45° away from the normal direction. The RE texture emerges during the nucleation of recrystallised grains and is maintained during subsequent uniform grain growth, which results in a stable RE texture being developed as recrystallisation progresses. The uniform grain growth could be attributed to solute drag suppressing the grain boundary mobility of those grains that had recrystallised with a basal texture and precipitate pinning restricting potential orientated grain growth.

1. Introduction

Pure Mg and Mg alloys commonly have a sharp basal crystallographic texture after cold or thermomechanical processing [1–5]. Subsequent annealing involving grain growth usually strengthens the texture intensity [6,7]. Various thermomechanical processing and alloying approaches have been employed to weaken the strong deformed texture [8–11]. The most encouraging discovery was that the addition of rare earth (RE) elements into pure Mg or conventional Mg alloy systems can effectively weaken the texture due to the appearance of a new texture component during thermomechanical processing and/or subsequent annealing [1,9,10,12–15]. Because this new texture component can be only found in Mg-RE alloys in most cases, it has been defined as "RE texture" [13]. Frequently reported RE textures are the ⟨11$\bar{2}$1⟩//ED (extrusion direction) produced after extrusion, and peak texture intensity reduced and tilted towards the transverse direction (TD) after rolling and/or subsequent annealing [2,16,17].

RE textures normally reduce the basal texture intensity, anisotropy and asymmetry of Mg alloys. Consequently, these alloys can be deformed more homogeneously with improved formability [13,18]. However, the exact origin of RE texture is still a matter of debate. So far, numerous potential proposed mechanisms of RE texture formation have been reported. The factors in these hypotheses include the choice of preferential nucleation sites [2,4,9,12,13,19–21], increased activity of pyramidal <c+a> slip [5], oriented grain growth and solute drag or particle pinning along some specific grain boundaries (GBs) [22–25]. It is impossible to elucidate and validate all the potential mechanisms in one piece of experimental work. Therefore in this work, we only address the issue of which nucleation site(s) and/or subsequent growth of corresponding recrystallised grains is(are) directly related to the RE texture formation.

Deformed GBs, shear bands, deformation twins and second phase particles are the four proposed recrystallisation nucleation sites [10,20,22,26–28]. There is a consensus that the latter three sites can produce recrystallised grains with a wide range of orientations and randomise the basal texture [1,10,22,25]. However, there is no agreement which nucleation site is the main source that produces grains with RE texture orientations. Moreover, the growth of recrystallised grains at individual nucleation sites remains a

* Corresponding author.
E-mail address: m.rainforth@sheffield.ac.uk (W.M. Rainforth).

http://dx.doi.org/10.1016/j.actamat.2017.06.015

challenging puzzle, and therefore the contribution that each makes to the full recrystallised texture is still a wide open question [1,10]. A variety of nucleation sites commonly coexist in Mg alloys after deformation, which makes it difficult to identify how recrystallised grains evolve from an individual nucleation site. Although particle stimulated nucleation (PSN) can be ignored in dilute Mg alloys or solid solution treated Mg alloys, deformation twins usually accompany shear bands in Mg-RE alloys where RE texture is also observed [18,21,25]. It is not clearly known whether recrystallisation in shear bands or twins is mainly responsible for RE texture formation. The unavoidable coexistence of twins and shear bands in most of the experimental cases makes it difficult to address this question. Therefore, to clarify the exact origin of RE texture, it is logical to design experiments to individually investigate the effect of shear bands and twins.

In our previous study [12] we showed that double twins (DTWs) can act as preferential nucleation sites for recrystallisation and the recrystallised grains originating from DTW-DTW and DTW-GB intersections can grow beyond the twin boundaries and expanded into deformed parent grains. Therefore, DTWs made the main contribution to the recrystallised texture, which contrasts the opposite view that has dominated in the past decades that recrystallisation in twins makes only a limited contribution [10,22,29–31]. Nevertheless, because the grain size was very large and therefore the examined area had only limited grains, the recrystallised texture may not have fully represented the bulk sample. Furthermore, some research reported the recrystallised texture also depends on subsequent growth of recrystallised grains [6,7,20,27,32], and so the debate remains: when does the RE texture orientation selection process occur [1,10]? During nucleation or the following grain growth stage?

To address these fundamental questions, we investigated the entire recrystallisation process from the as-cold rolled state to full recrystallisation condition of a Mg-RE alloy. The prior solid solution treatment and cold rolling process were intentionally adjusted to ensure that double twins were the dominant deformation feature in this work. We successfully employed a *quasi-in-situ* EBSD method to allow a site-specific method to track the recrystallisation process at each point in the microstructure and therefore to follow the nucleation at DTWs, subsequent recrystallised grain growth and texture evolution. To the best of our knowledge, this work for the first time provided direct evidence that recrystallised grains originating from double twins can form RE texture during annealing. The RE texture orientation selection took place during the nucleation process and grew uniformly during the subsequent grain growth stage. The individual role of shear bands on the texture weakening was excluded in the current work, but will be reported in a separate paper. These findings have filled some fundamental gaps mentioned in two recent review papers discussing the origin of RE textures [1,10] and could shed light on designing new wrought Mg alloys and optimising the thermo-mechanical processes to improve formability of commercial Mg alloys.

2. Experimental procedure

The alloy examined is the same as used in Ref. [12]. A rectangular plate 50 (ED) × 25 × 6 mm^3 was cut from the extruded bar for heat treatment and cold rolling. Solid solution treatment was carried out in a tube furnace with a continuous argon flow at 525 °C for 1 h (SST1H), followed by cold water quenching. The SST1H sample was then cold rolled with a reduction of 20% in one pass. The EBSD sample procedure can be found in Ref. [12].

EBSD was performed using a FEI Nano Nova 450 field emission gun SEM fitted with Oxford Instruments HKL NordlysMax^3 EBSD detector. The EBSD data were analysed via using HKL CHANNEL5 software. Fiducial marks were made on the surface of the cold-rolled sample after OPS polishing. Thus the area scanned for EBSD was relocated after further annealing to allow re-scanning of the same area. The *quasi-in-situ* EBSD collected data from a large area of about 1.4 mm^2 from the middle part of RD-ND plane. The EBSD scans were taken after cold rolling and after 5, 12, 21, 39, 90, 114, 163, 242, 341, 520, 920, and 1520 min annealing at 490 °C. The details of *quasi-in-situ* EBSD procedure were listed in Ref. [12].

3. Results

3.1. Microstructure after solid solution treatment and cold rolling

The as-received extruded sample microstructure was reported in Ref. [12]. Fig. 1 presents a large scale EBSD Inverse Pole Figure (IPF) map of the SST1H sample. The average grain size was found to be 82.3 μm. The inset (0002) pole figure (PF) indicated a majority of grains in the SST1H sample had their basal (0001) plane parallel to the ED. However, the intensity of 6.5 multiples of uniform density (mud) was lower than that in conventional non-RE Mg alloys [6,31,33].

Fig. 2(a) shows a backscattered SEM image of the SST1H sample after cold rolling for *quasi-in-situ* EBSD experiment subjected to 20% thickness reduction in one pass. Although the solution treatment time was only 1 h, nearly all the initial intermetallic compounds dissolved into the matrix except some sparsely distributed RE enriched particles, which were also shown in samples after 24 h solid solution treatment [12]. Therefore, the effect of second phase particles on the recrystallised texture would have been negligible. Moreover, Robson et al. [19] investigated the texture of the recrystallised grains originating from second phase particles via particle stimulated nucleation (PSN) appears to be random. Imandoust et al. [1] also stated the PSN recrystallisation mechanism could not be treated as a main source of RE texture, since PSN normally produces random texture.

Fig. 2(b) gives a corresponding band contrast (BC) image and shows that deformation twins can be clearly found in nearly all deformed grains. To identify twin types, the special boundary component has been superimposed. Fig. 2(c) presents the distribution of misorientation angles between neighbouring points in this map. In addition to the low misorientations associated with low angle GBs, there were two peaks around 38° and 86°

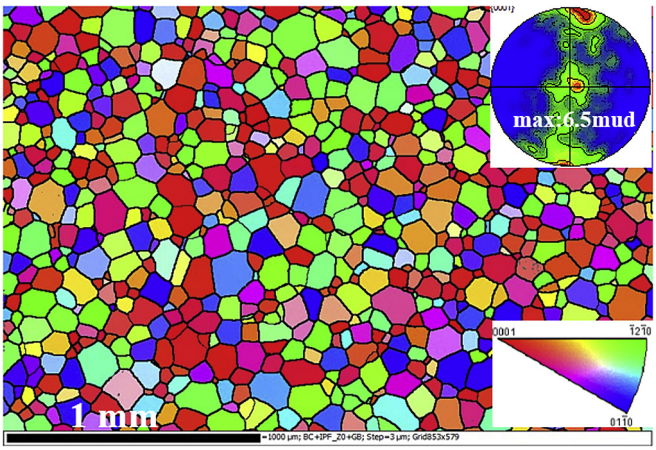

Fig. 1. EBSD IPF image of sample SST1H. The insets are corresponding (0002) pole figure and legend of IPF map. The extrusion direction (ED) is horizontal and observation along radial direction was applied to IPF triangle. (0002) pole figure is shown in the same orientation as the corresponding map.

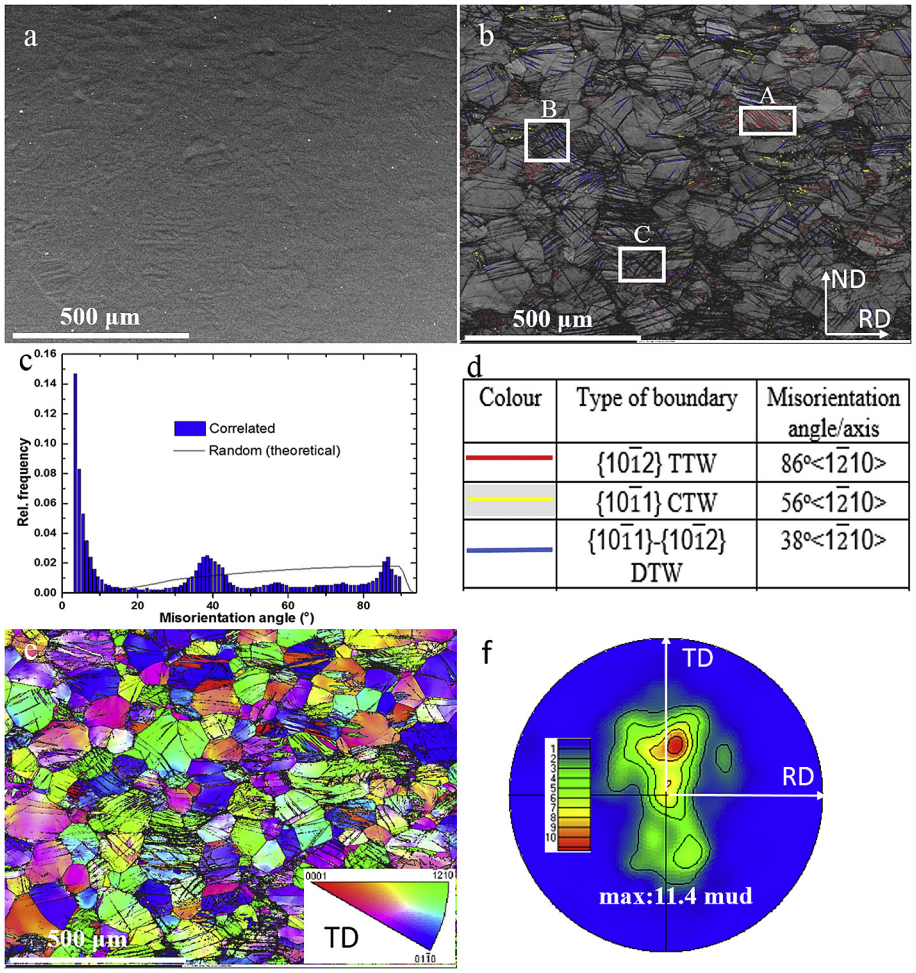

Fig. 2. (a) Backscattered SEM image of cold-rolled sample SST1H (b) corresponding band contrast (BC) map superimposed by various twin boundaries, (c) misorientation angle distribution, and (d) the most common twin types in this cold-rolled sample, (e) corresponding IPF map, and (f) (0002) pole figure. Observation along TD was applied to IPF triangle.

representing two types of twin boundaries. Fig. 2(d) lists the main twin types present in this specimen according to Fig. 2(b–c). The dominant twin boundaries are double twins (DTWs) and tension twins (TTWs). The number of compression twin (CTW) boundaries was limited due to the rapid transformation of CTW to DTW fragments by secondary {10$\bar{1}$2} twinning [34]. The non-indexed regions in the EBSD are associated with high local strain areas such as areas within twins and twin-GB intersections. These non-indexed twins can be determined as DTWs. Firstly, the shape was similar and orientations were close to adjacent indexed DTWs. Secondly, extensive basal slip is known to occur within correctly oriented DTWs resulting in significant lattice distortion and local strain [20,32,33], which makes DTWs difficult to be indexed. Thirdly, because basal slip is not favoured in TTWs and its twin boundaries are highly mobile compared to DTWs or CTWs [10,20,35,36], the magnitude of local strain is expected to be much lower in TTWs than DTWs. Hence, TTWs are usually indexed in EBSD, [12,20,25,37]. Fig. 2(e) shows an IPF map and the corresponding (0002) PF is shown in Fig. 2(f). Two texture peaks were observed in the pole figure: the strongest one of 11.4 mud around 30° towards the TD direction and the other a strong basal texture with intensity of 7.9 mud.

3.2. Nucleation and recrystallised grain growth

Fig. 3(a–l) presents the entire recrystallisation process from nucleation to complete recrystallisation. These sequential EBSD maps as a function of annealing time allowed us to exactly locate the origin of the recrystallised grains as well as follow their subsequent growth. After 5 min annealing as shown in Fig. 3(a), small recrystallised grains were readily observed at DTW and non-indexed DTW-GB intersections. Fig. 3(b) shows that recrystallisation had occurred in all the DTWs after annealing for 12 min, and no recrystallisation occurred along deformed GBs except where they were intersected by the end of DTWs. This is in agreement with the recrystallisation behaviour reported in our previous study, namely that DTWs are the preferential site for recrystallisation in WE43 alloy [12]. To further confirm this conclusion in the current study, representative high magnification images from small areas marked A, B and C shown in Fig. 2(b) are provided in Fig. 4. Fig. 4(a) presents a deformed grain consisting of TTWs. After annealing for 5 min (Fig. 4(b)) and 12 min (Fig. 4(c)), the recrystallised grains that can be seen in the bottom images had come from another deformed grain and no recrystallisation occurred around TTWs, in agreement with the results in Refs. [12,20]. Fig. 4(d) and (g) show regions that mainly contain DTWs and DTW-GB intersections. After 5 and 12 min annealing, new grains nucleated around these sites (Fig. 4(e, h)) and started to grow towards adjacent deformed parent grains (Fig. 4(f, i)). More detailed high resolution EBSD images of this process are presented in Ref. [12].

With annealing ranging from 21 to 1520 min, the recrystallised grains started to grow and consume all the adjacent deformed

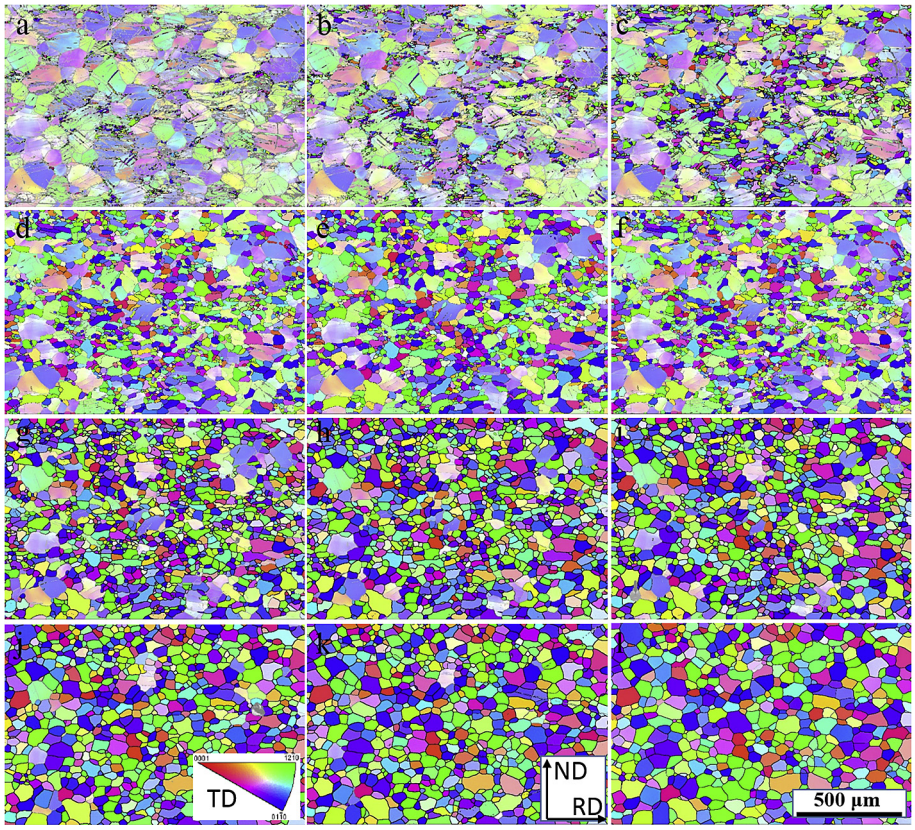

Fig. 3. EBSD IPF subset maps only showing recrystallised grains mainly around DTWs and DTW-GB intersections at annealing intervals of (a) 5, (b) 12, (c) 21, (d) 39, (e) 90, (f) 114, (g) 163, (h) 242, (i) 341, (j) 520, (k) 920, and (l) 1520 min. The axes systems are all the same as shown in Fig. 3(k). Observation along TD was applied to IPF triangle.

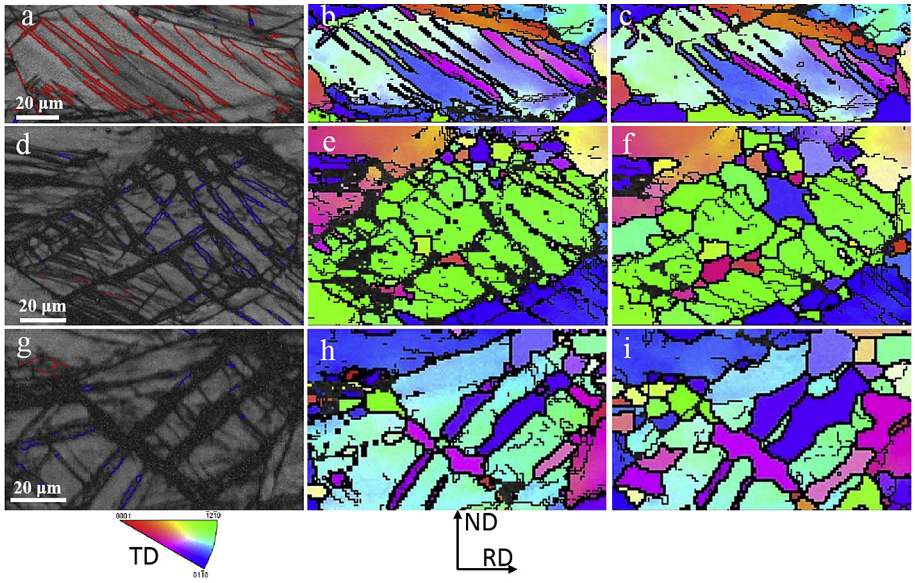

Fig. 4. (a) EBSD BC map containing TTWs after cold rolling, corresponding IPF map after (b) 5 and (c) 12 min; (d) EBSD BC map containing DTW-DTW and DTW-GB intersections after cold rolling, corresponding IPF map after (e) 5 and (f) 12 min; (g) EBSD BC map mainly containing DTW-DTW intersections after cold rolling, corresponding IPF map after (h) 5 and (i) 12 min. Observation along TD was applied to IPF triangle.

grains. Although there were some recrystallised grains nucleating from GBs in the late annealing stage, the recrystallised grains originating from DTW-DTW and DTW-GB intersections occupied the vast majority of recrystallised areas during the whole annealing process.

Fig. 5 plots the recrystallised volume fraction as a function of annealing time at 490 °C. After 5 min annealing, the recrystallised volume fraction was only 7.3% due to an incubation period before recrystallisation. Subsequently, the recrystallisation rate increased quickly after annealing for 12 min. The recrystallised volume

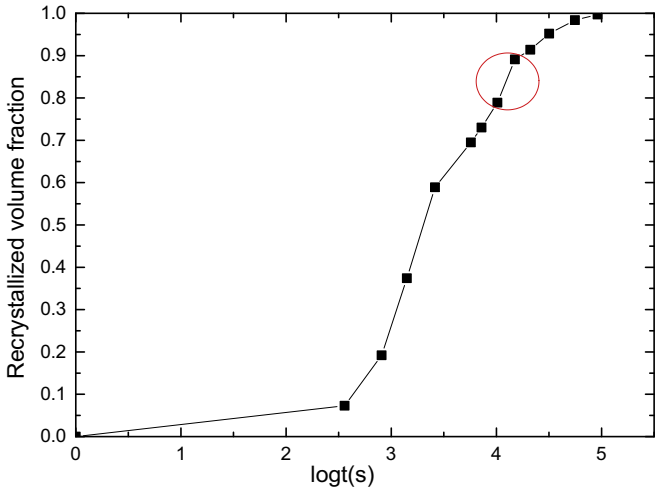

Fig. 5. Recrystallised volume fraction as function of annealing time (an abnormal recrystallisation rate was marked by a red circle). (For interpretation of the references to colour in this figure legend, the reader is referred to the web version of this article.)

fraction was 19.2%. During the subsequent early grain growth stage, the increased recrystallisation rates resulted in growth of recrystallised volume fraction to 37.4% and 58.9% after annealing for 21 and 39 min respectively. Through the later grain growth stage, recrystallised grains started to impinge and the deformed areas were largely consumed, leading to a gradual decrease in the recrystallisation rate. The recrystallised volume fraction was 69.5% after 90 min but it took 341 min to reach a recrystallised volume fraction of 91.4%, while full recrystallisation was almost reached after annealing for 1520 min. It is notable that there was a disproportionate increased recrystallisation rate between 163 and 242 min (red circle in Fig. 5) over and above that expected from Avrami kinetics [27].

3.3. Texture evolution of all recrystallised grains during annealing

The commonly used (0002) pole figure (PF), taken from only the recrystallised grains, was collected from Fig. 3(a–l) and given in Fig. 6(a–l). Fig. 6(a) shows a PF after 5 min annealing during which time there was significant nucleation of recrystallisation. The PF shows two separate texture peaks situated away from the centre basal texture and towards the TD directions, either side of the vector pointing to the TD pole, which is a typical RE texture after rolling in Mg-RE alloys [1,10]. After 12 min annealing, the RE texture morphology had not significantly changed (Fig. 6(b)). With 21 min annealing, growth of recrystallised grains had clearly occurred (Figs. 3(c) and 5). The RE texture was largely unchanged, as shown in Fig. 6(c), with the texture intensity located in the lower part of the PF weaker than the upper part. For longer annealing times the RE texture was well defined and did not measurably change up to near full recrystallisation at 1520 min, as shown in Fig. 6(d–l). The only observable change was the texture component intensity of the upper part of the pole figure strengthened slightly. Therefore, Fig. 6 unequivocally indicates that the RE texture appeared at the nucleation stage and was maintained during the whole recrystallisation process.

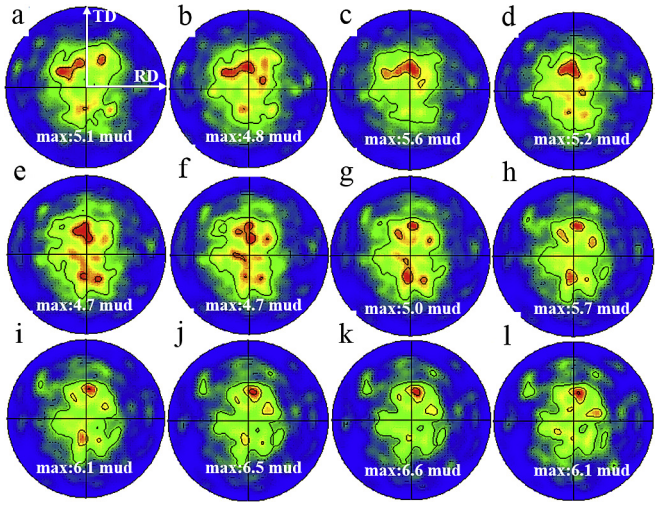

Fig. 6. (0002) pole figures consisting only of recrystallised grains mainly formed at DTWs and DTW-GB intersections at annealing intervals of (a) 5, (b) 12, (c) 21, (d) 39, (e) 90, (f) 114, (g) 163, (h) 242, (i) 341, (j) 520, (k) 920, and (l) 1520 min. The axes systems are all the same as shown in Fig. 6(a).

3.4. Evolution of individual texture components during annealing

To explore whether grains with specific orientations grow preferentially during annealing, the recrystallised grains were divided into four groups based on the angle differences between their c-axis and ⟨0001⟩ basal texture (the tilt of basal poles away from ND). These four groups were 0–20°, 20–45°, 45–70° and 70–90° tilting away from ND and were designated as texture component A (TCA), texture component B (TCB), texture component C (TCC) and texture component D (TCD) in the following sections.

Figs. 7–10 provide a series of EBSD IPF subset maps of the TCA, TCB, TCC and TCD grains, respectively, which clearly show the texture evolution of recrystallised grains throughout the entire recrystallisation process. The insets in all the sets of Figs. 7–10 are corresponding (0002) PF. Small recrystallised grains in each texture component were consumed by other texture components in the later grain growth stage, e.g., grain 1 in Fig. 7, grain 2 in Fig. 8, grain 3 in Fig. 9 and grain 4 in Fig. 10. For grains with TCA orientations, grains were orientated relatively homogeneously within the region of 0–20° tilted away from the ND and the peak texture intensity fluctuated around 20 mud (Fig. 7). For grains with TCB orientations, grains were preferentially oriented towards the TD directions at the start of recrystallisation and this did not change throughout the whole recrystallisation process. The peak texture intensity varied around 10 mud (Fig. 8). Fig. 9 shows grains with the TCC orientation exhibited a generally uniform distribution between the TD and RD during the entire annealing process, with a texture intensity in the range from 6.9 to 11.4 mud. However, for TCD grains (Fig. 10), the orientation of the strongest texture component changed significantly with respect to the TD and RD, although the number of grains sampled was low.

Recent published work suggested oriented grain growth played a significant role in modifying the recrystallised texture [4,22,25]. Fig. 11 shows the average grain size of recrystallised grains of each texture component as a function of annealing time. The mean grain size followed almost the same trend for all the four groups from 5 to 39 min annealing, and showed no difference between TCA, TCB and TCC grains, even after 242 min annealing. The TCA and TCB grains had a similar mean grain size throughout the whole recrystallisation process. Fig. 12(a) provides number of recrystallised grains of each texture component as a function of annealing time. TCB contained the most grains during the entire recrystallisation process, followed successively by TCC, TCA and TCD. The number of recrystallised grains reached a peak after 12 min annealing when the nucleation stage was believed to be complete and decreased

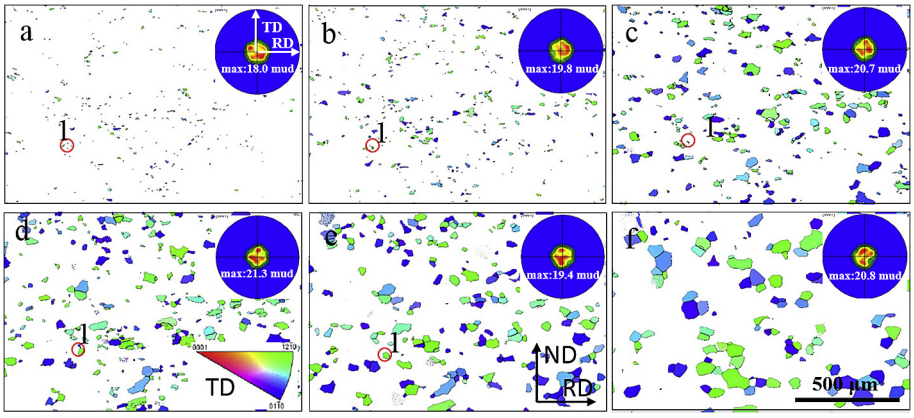

Fig. 7. EBSD IPF subset maps showing the growth of recrystallised grains from texture component TCA at annealing intervals of (a) 5, (b) 12, (c) 39, (d) 114, (e) 242 and (f) 1520 min. The axes systems are all the same as shown in Fig. 7(e). Observation along TD was applied to IPF triangle.

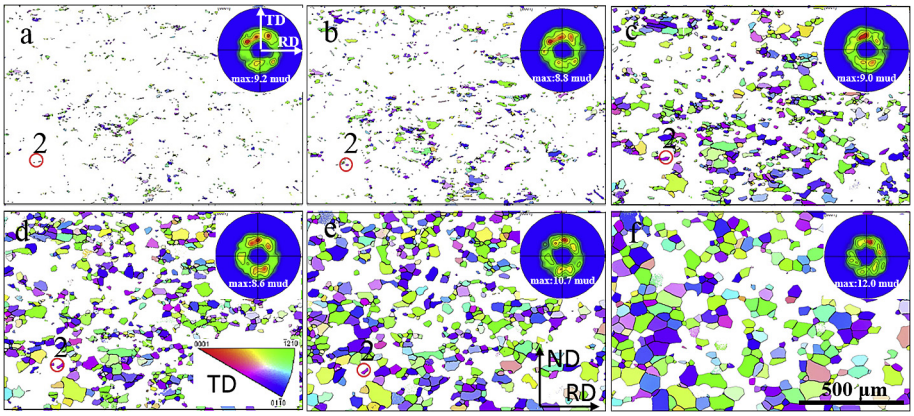

Fig. 8. EBSD IPF subset maps showing the growth of recrystallised grains from texture component TCB at annealing intervals of (a) 5, (b) 12, (c) 39, (d) 114, (e) 242 and (f) 1520 min. The axes systems are all the same as shown in Fig. 8(e). Observation along TD was applied to IPF triangle.

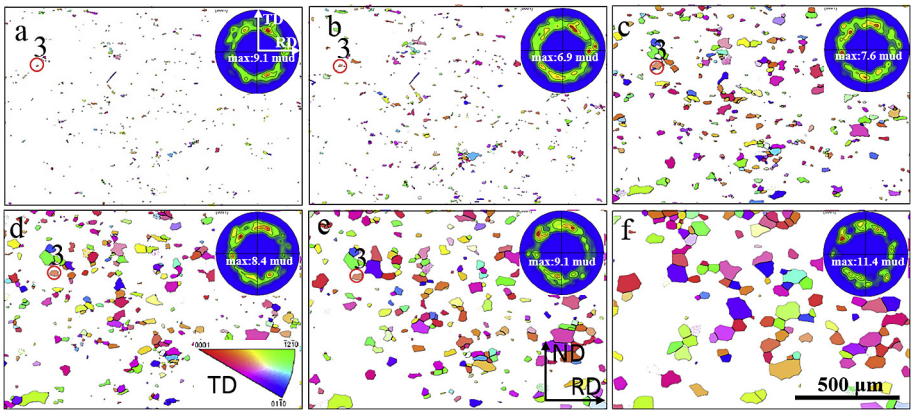

Fig. 9. EBSD IPF subset maps showing the growth of recrystallised grains from texture component TCC at annealing intervals of (a) 5, (b) 12, (c) 39, (d) 114, (e) 242 and (f) 1520 min. The axes systems are all the same as shown in Fig. 9(e). Observation along TD was applied to IPF triangle.

thereafter for longer annealing times showing that grain growth was the dominant process (Figs. 3 and 5). The number fraction of recrystallised grains of each texture component based on the total number of recrystallised grains after each annealing interval is shown in Fig. 12(b). The recrystallised grain number fraction of every texture component was comparatively stable throughout the entire annealing process. This is important as it indicated that grain consumption did not depend on a particular orientation.

Fig. 13(a) plots the recrystallised volume fraction of each texture component during annealing. The recrystallised volume fraction of each texture component as a function of the total volume of material exhibited similar Avrami kinetics, as expected. This plot suggests the TCB texture component was dominant, consuming around 51% of the total volume at the completion of

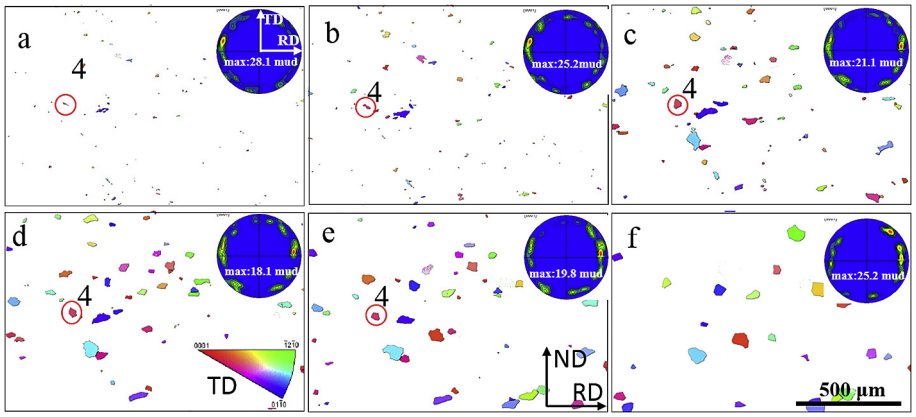

Fig. 10. EBSD IPF subset maps showing the growth of recrystallised grains from texture component TCD at annealing intervals of (a) 5, (b) 12, (c) 39, (d) 114, (e) 242 and (f) 1520 min. The axes systems are all the same as shown in Fig. 10(e). Observation along TD was applied to IPF triangle.

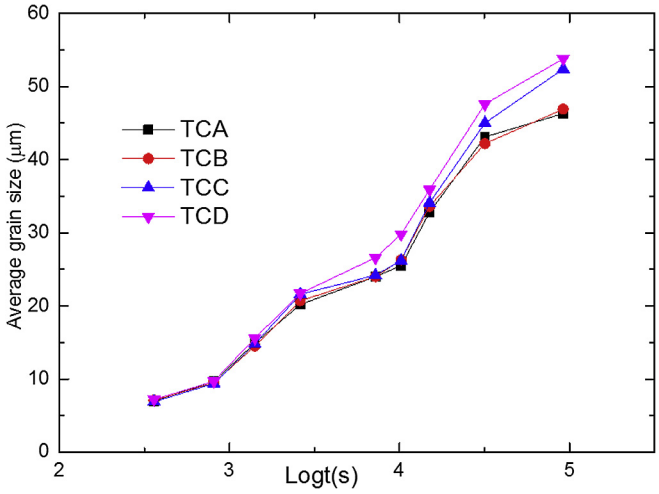

Fig. 11. Average grain size of each recrystallised texture component as a function of annealing time.

recrystallisation, i.e. more than the other three components put together. Moreover, the (0002) PF of the TCB component was very close to the defined RE texture after rolling. Fig. 13(b) gives the volume fraction of each texture component plotted as fraction of the total recrystallised area only, rather than the whole mapped area that was used in Fig. 13(a). Although there were significant differences in the recrystallised volume fractions from each component, the volume fraction of each texture component did not vary greatly during growth of the recrystallised grains, which was in agreement of the results presented in Fig. 12(b). It might be proposed that the RE texture formation was attributed to the oriented grain growth of texture component TCB based on the results of Fig. 13 (a). However, as shown in Fig. 11, the average grain size of the TCB component was very similar to the other three groups during most of the annealing time and smaller than TCC and TCD in the late annealing stages. The large portion of TCB recrystallised fraction (Fig. 13(b)) was due to the high number of grains and high grain number fraction with this orientation produced during nucleation stage (Fig. 12) and was preserved during the subsequent growth stage due to uniform grain growth (Figs. 11 and 12(b) and 13(b)).

3.5. Precipitation during recrystallisation

To explore the mechanism of static recrystallisation retardation along deformed GBs, detailed investigations along GBs during annealing was undertaken. A *quasi-in-situ* SEM method using a backscattered detector was employed to track the microstructural evolution around prior GBs within the same area. Fig. 14(a) presents a typical sampling area of an EBSD band contrast map after cold rolling and Fig. 14(b) is the kernel average misorientation (KAM) map. The unindexed black regions have the greatest lattice distortion and thus have higher local misorientation than those areas that have been indexed. Fig. 14(c) shows the corresponding microstructure in the same area of Fig. 14(a) after 12 min annealing. All the prior GBs and twin boundaries with high local strain were decorated by small precipitates while these boundaries did not

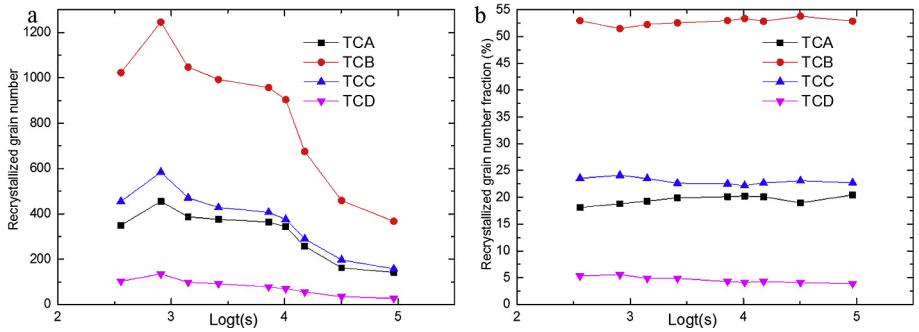

Fig. 12. (a) Recrystallised grain number of each texture component and (b) recrystallised grain number fraction of each texture component based on the whole recrystallised grain number as a function of annealing time.

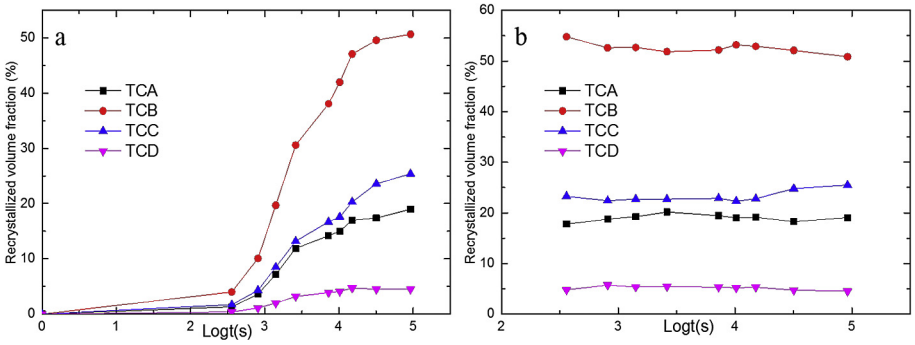

Fig. 13. (a) Recrystallised volume fraction of each texture component based on the whole sampling area including recrystallised and deformed regions, and (b) recrystallised volume fraction of each texture component based only on the recrystallised area as a function of annealing time.

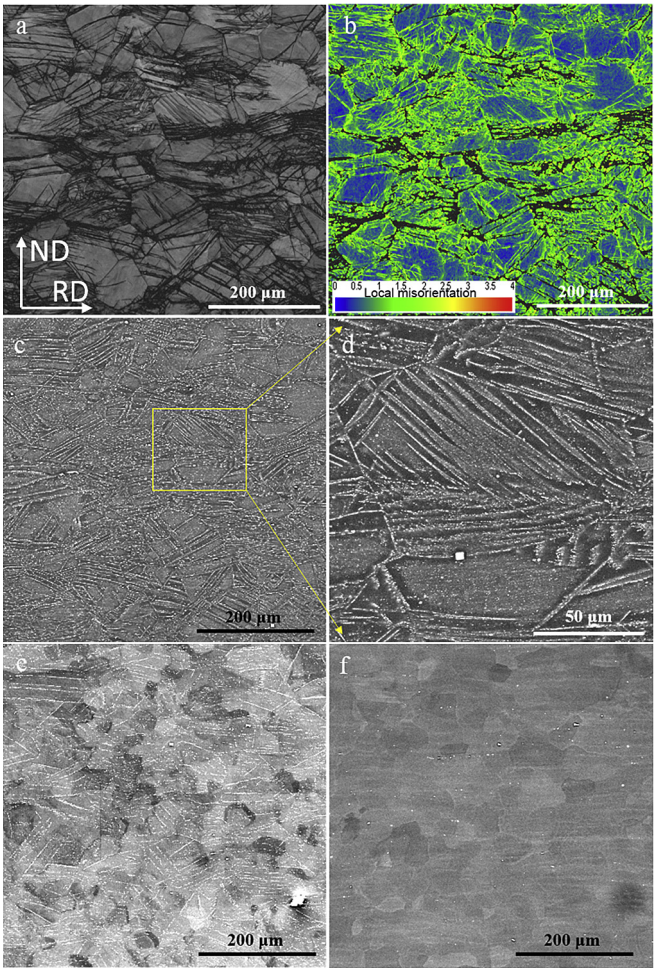

Fig. 14. (a) EBSD band contrast (BC) map of sample SST1H, (b) corresponding KAM map of (a) showing the stored energy distribution (The non-indexed areas have the highest local strain) (c) *Quasi-in-situ* backscattered SEM images at annealing intervals of 12 min and (d) corresponding high magnification, (e) 163 min and (f) 242 min.

contain precipitates before annealing (Fig. 2(a)). The area marked in Fig. 14(c) was magnified so that precipitates along all the boundaries can be clearly distinguished, shown in Fig. 14(d). With further annealing, this precipitation process continued and particle coarsening also occurred. Fig. 14(e) shows these precipitates still exist along the prior boundaries after annealing for approximately 163 min, but most had disappeared during growth of recrystallised grains. After annealing for 242 min when the recrystallised volume fraction was 89% (Fig. 5), all the precipitates had dissolved into the matrix (Fig. 14(f)).

4. Discussion

4.1. Mechanism of retarded static recrystallisation along GBs

As proposed in Refs. [1,10], deformed GBs, deformed twins, shear bands and second phase particles are the four main nucleation sites for recrystallisation in Mg alloys. The effect of particle stimulated recrystallisation on RE texture evolution can be excluded in this work since solid solution treatment removed the majority of the particles and PSN does not form unique types of crystal orientations [1,19] and could not be responsible for the RE texture orientation observed in this work. Equally, the effect of shear bands on recrystallisation could be excluded as the material was processed in such a way as to avoid the formation of shear bands. Therefore, nucleation of recrystallisation should only occur in twins and at prior GBs. However, as shown in Fig. 3, most of the grain boundaries were not effective nucleation sites and recrystallisation did not occur along most GBs. The exception to this was where the local strain was higher, in particular, where DTWs intersected the grain boundary. There is a consensus that the GB recrystallisation occurs by strain induced grain boundary migration (SIBM) during isothermal annealing, which was first reported by Beck and Sperry [38]. In this study, limited evidence of SIBM was found.

Recently, a solute drag mechanism was proposed and successfully explained the retardation of dynamic recrystallisation in Mg-RE alloys with weakened basal texture. RE elements with a large atom size preferably segregate along GBs and inhibit boundary movement [24,39–41]. However, solute drag is predicted to be insufficient to totally restrict static recrystallisation. For example, the solute drag exerted in a Mg-12Y (wt.%) alloy with maximum solubility was calculated to be smaller than half the estimated driving pressure for static recrystallisation at any temperature higher than 250 °C [24]. Moreover, the solute drag pressure drops sharply with increasing temperature [42]. In the current work, it is not clear whether solute drag contributed to inhibiting static recrystallisation as the situation was complicated by the occurrence of precipitation, as discussed below.

An unusual precipitation phenomena was observed at high annealing temperature of 490 °C, with precipitates forming on twin and grain boundaries, but the precipitates subsequently dissolved, Fig. 14. This precipitation phenomenon is described in detail elsewhere recently where it was studied using *in-situ* TEM [43]. This unusual precipitation around the solid solution temperature has also been observed in an AZ81 Mg alloy, where it was believed that the deformation changed the precipitation kinetics and caused

strain induced precipitation [44]. This preferential precipitation along prior boundaries could be attributed to the higher dislocation density and higher local strain around these boundaries than in the deformed grain interiors, Fig. 14(b), and so the precipitation could reduce the internal system energy. Clearly, these temporary precipitates can account for the retardation of recrystallisation along prior GBs and abnormal increased recrystallisation rate in the late stage of grain growth when the precipitates had dissolved, shown in Fig. 5.

The interaction between precipitation and recovery and recrystallisation was clearly complex, leading to deviations from Avrami kinetics during recrystallisation. Humphreys and co-workers have studied this extensively in Al alloys [27,45]. Fig. 15, adapted from Ref. [27], presents a schematic time, temperature, transformation curve for recrystallisation and precipitation. Temperature points A and B shown in Fig. 15 are precipitation and recrystallisation interaction points. When the annealing temperature is lower than T_B, considerable precipitation would occur before recrystallisation and thereby inhibit recrystallisation. When the annealing temperature is between T_B and T_A, recrystallisation and precipitation occur simultaneously. The precipitates will decrease the recrystallisation rate and delay full recrystallisation. When the annealing temperature is higher than T_A, full recrystallisation occurs before precipitation, and therefore the recovery and recrystallisation mechanisms will not be altered [27,45]. Combining this schematic with the experimental results in this work, the annealing temperature of 490 °C is between T_B and T_A. During annealing, areas or boundaries with the highest stored energy were particularly favoured for recrystallisation, i.e., DTWs in this work, since high dislocation density introduced by intensive basal slip in soft orientated thin DTWs results in the DTWs becoming preferential sites for recrystallisation. This effect is further improved around DTW-DTW and DTW-GB intersections [12,20,30]. On the other hand, the precipitates pinned the prior GBs and inhibited recrystallisation along GBs, which indirectly facilitated the RE texture formation, since recrystallised grains introduced by SIBM along prior GBs usually have basal orientations [1,10,22,25].

4.2. Mechanism of RE texture formation during annealing

The disputed question of whether RE texture forms during nucleation or subsequent growth of the recrystallised grains can be answered with reference to Fig. 6. The RE texture orientations were clearly generated during the nucleation of recrystallisation. Although the peak texture intensity varied after each subsequent annealing, the RE texture morphology was well preserved during the growth of recrystallised grains, even after full recrystallisation. The grain size of TCD orientation appeared to grow fast compared to TCB grains in the late stage, but the negligible volume fraction of the TCD grains meant that they had little effect on the overall texture. The question therefore is how this RE texture emerged and sustained during the whole recrystallisation process.

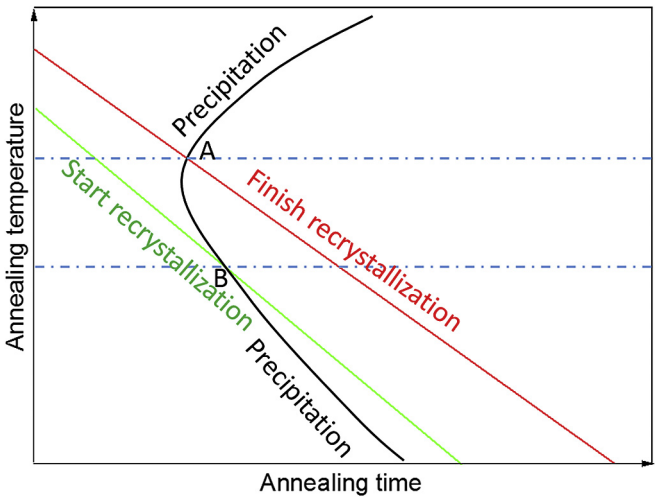

Fig. 15. A schematic for illustrating the interactions of precipitation and recrystallisation during isothermal annealing, adapted from Ref. [27].

4.2.1. Appearance of RE texture at nucleation

CTWs and DTWs were reported to nucleate recrystallised grains with RE orientations [10,46,47]. In this study, most nucleation sites including shear bands, GBs, second phase particles, CTWs and TTWs either made limited contribution or were not present in the deformed structure and therefore did not contribute to the recrystallised texture. The appearance of the RE texture after 5 min annealing (Figs. 3(a) and 6(a)) occurred from recrystallisation taking place in the DTWs. However, the nucleation of recrystallised grains within these twins cannot guarantee the final RE texture after full recrystallisation, i.e. it is not always the case that these grains survive through to the end of full recrystallisation. Chatterton et al. showed that in a similar Mg-RE alloy deformed by cold wire drawing that contained CTWs and DTWs, the distinctive RE texture was not observed after full recrystallisation [48]. The possible reason for this is that the RE texture evolution also depends on growth of recrystallised grains with RE orientations. Guan et al. [12] systematically studied recrystallisation occurring in DTWs and DTW-GB intersections during the early stage of annealing. However, during subsequent growth, the recrystallised grains within the individual DTW lamellae were constrained and consumed by the other recrystallised grains, and so they did not make a contribution to the final texture. In contrast, recrystallised grains originating from DTW-DTW and heavily deformed DTW-GB intersections readily grew into the deformed parent grains. Therefore, whether recrystallisation originating from DTWs makes a contribution to the final texture depends strongly on the initial DTWs distribution morphology and density. The number of CTWs and DTWs observed in a cold worked microstructure decreases substantially with decreasing grain size [37]. The average grain size of cold drawing sample obtained by Chatterton et al. [48] was only ~10 μm, while the grain size of the material in the current work was ~82 μm. Therefore, the density of CTWs (which were usually rapidly transformed into DTWs [34]), DTWs and related DTW-DTW intersections were much lower in the work of Chatterton et al. [48] than in our study. This explains why the recrystallised grains from DTW-DTW and heavily deformed DTW-GB intersections were the main component of recrystallised texture in the current study while recrystallised grains from CTWs and DTWs in Chatterton et al.'s work [48] may have made only limited contribution to texture or may have been consumed by recrystallised grains from other nucleation sites, such as GBs or second phase particles. We have shown in work to be published separately where a microstructure was generated with only a minor presence of DTW-DTW and heavily deformed DTW-GB intersections, the recrystallised grains from DTWs only occupied ~4% of the whole recrystallised volume fraction after full recrystallisation. Thus, the prior grain size has a strong effect on the contribution of recrystallisation from DTWs to the RE texture formation.

4.2.2. Effect of solute segregation on RE texture evolution

The large size of RE atoms relative to Mg leads to segregation of RE atoms to GBs. The formation of the RE texture has been reported to have a strong relationship with the associated solute drag [1,4,10,25,39–41,49]. This is used to explain why the RE texture

appeared when the extrusion temperature was below 500 °C but disappeared when the temperature was above 500 °C in a Mg-Gd alloy [49] since solute segregation to GBs was much less above this temperature. These results demonstrated how solute drag restricted prior GB mobility, retarded dynamic recrystallisation along prior GBs and thereby played a critical role in producing the RE texture. Although solute drag may not retard static recrystallisation effectively at high temperature, it could slow down the recrystallised GBs mobility during the subsequent grain growth stage [1,24,25,39]. Basu et al. [25] and Zeng et al. [22] found the solute pairs or co-segregation exerted stronger solute drag than single solute in dilute Mg alloys. The enhanced drag effect further decreased the GB mobility of recrystallised basal oriented grains, thereby suppressing their preferential growth resulting in a weak basal texture [22,25]. For the WE43 used in this study contained a greater amount of RE elements than in the samples used by Refs. [22,25], and therefore significant solute drag would be expected to have been important in the RE texture formation. However, it is far from clear to know the extent of solute drag, since it is believed that pinning of the grain boundaries by precipitation would have had a more important effect, as discussed below.

4.2.3. Simultaneous precipitation on grain growth and RE texture evolution

The main difference between the current work and other studies of RE texture evolution was the unexpected occurrence of precipitation during annealing. Dilute solid solution treated Mg-RE alloys, in which precipitation did not occur during sample processing, have exhibited various textures after annealing. Some studies reported an RE texture [10,13,40,41,47,50], while other reports did not find a significant texture change compared to the as-deformed texture [4,49,51]. Although it is disputed which factors were responsible for the difference in texture evolution, it is clear that precipitation during recrystallisation does not have a critical role in forming RE texture since an RE texture is observed in alloys where precipitation does not occur. Nevertheless, the connection between precipitation and recrystallised grain growth merits further investigation.

As shown in Fig. 14 and also observed in our recent study [43], precipitation occurred along twin and grain boundaries in the early stage of recrystallisation. Subsequently, these precipitates coarsened and eventually re-dissolved. Although all the twins were consumed during recrystallisation, the precipitates did restrict grain growth perpendicular to the original twin boundaries [43], thereby constraining the size of some recrystallised grains to that of the pre-existing twin boundaries. This reduction in grain growth would have restricted the potential for growth of specific crystal orientations. Figs. 11–13 show that all the grains from all four texture components had a similar grain size after nucleation and grew uniformly during subsequent growth. This indicates that precipitate pinning affected all crystal orientations equally. These results are in agreement with Chatterton et al.'s work [48] where a similar alloy was studied and no orientation specific grain growth was found.

The precipitates distributed along prior deformed GBs were shown to retarded recrystallisation along GBs by restricting the SIBM mechanism. This would have been expected to considerably reduce the number of grains with a basal texture. Therefore the precipitation on grain boundaries was beneficial for producing RE texture.

5. Conclusions

The entire recrystallisation process during annealing was tracked using a *quasi-in-situ* EBSD method. The nucleation and subsequent grain growth were followed in a site specific manner. The individual effect of double twinning on texture weakening in this alloy was investigated in detail, and the main conclusions were drawn:

(1) $\{10\bar{1}1\}$-$\{10\bar{1}2\}$ double twins (DTWs), especially DTW-DTW and DTW-GB intersections, were the preferential nucleation sites for recrystallisation in the cold-rolled sample and made the main contribution to recrystallised texture.
(2) Precipitation and recrystallisation occurred simultaneously during annealing. Precipitates were preferentially formed along prior grain and twin boundaries. These precipitates pinned the GBs and caused the retardation of recrystallisation along GBs, which reduced the occurrence of recrystallised grains with the deformed basal texture and was therefore beneficial for RE texture formation.
(3) Because DTWs acted as the main nucleation sites and recrystallisation along GBs was retarded, it can be explicitly concluded that recrystallisation originating from DTWs accounted for the RE texture in this alloy. The RE texture appeared during nucleation of recrystallisation and remained constant during the whole of the grain growth stage. Overall, there were no evidence of preferential grain growth of specific crystal orientations, and most of the recrystallised grains grew uniformly. The uniform grain growth could be attributed to the solute drag suppressing the grain boundaries mobility of basal recrystallised grains and precipitate pinning restricting potential orientated grain growth.
(4) A large portion of recrystallised grains with ⟨0001⟩ poles 20–45° tilted away from the normal direction during entire annealing is due to the large number of grains nucleated with this orientation, followed by uniform grain growth rather than oriented grain growth. Although grains with basal poles tilted 70–90° away from the ND showed greater grain growth and had a relatively large average grain size, the negligible volume fraction would have only slightly affected the overall texture.

Acknowledgements

This work was funded by the EPSRC DARE Project, EP/L025213/1.

References

[1] A. Imandoust, C.D. Barrett, T. Al-Samman, K.A. Inal, H. El Kadiri, A review on the effect of rare-earth elements on texture evolution during processing of magnesium alloys, J. Mater. Sci. (2016) 1–29.
[2] T. Al-Samman, X. Li, Sheet texture modification in magnesium-based alloys by selective rare earth alloying, Mater. Sci. Eng. A 528 (2011) 3809–3822.
[3] J. Hirsch, T. Al-Samman, Superior light metals by texture engineering: optimized aluminum and magnesium alloys for automotive applications, Acta Mater. 61 (2013) 818–843.
[4] I. Basu, T. Al-Samman, G. Gottstein, Shear band-related recrystallisation and grain growth in two rolled magnesium-rare earth alloys, Mater. Sci. Eng. A 579 (2013) 50–56.
[5] S. Sandlöbes, S. Zaefferer, I. Schestakow, S. Yi, R. Gonzalez-Martinez, On the role of non-basal deformation mechanisms for the ductility of Mg and Mg–Y alloys, Acta Mater. 59 (2011) 429–439.
[6] J.J. Bhattacharyya, S.R. Agnew, G. Muralidharan, Texture enhancement during grain growth of magnesium alloy AZ31B, Acta Mater. 86 (2015) 80–94.
[7] M.A. Steiner, J.J. Bhattacharyya, S.R. Agnew, The origin and enhancement of texture during heat treatment of rolled AZ31B magnesium alloys, Acta Mater. 95 (2015) 443–455.
[8] X. Huang, K. Suzuki, Y. Chino, M. Mabuchi, Influence of rolling temperature on static recrystallisation behavior of AZ31 magnesium alloy, J. Mater. Sci. 47 (2012) 4561–4567.
[9] E.A. Ball, P.B. Prangnell, Tensile-compressive yield asymmetries in high strength wrought magnesium alloys, Scr. Metallurgica Mater. 31 (1994) 111–116.
[10] D. Griffiths, Explaining texture weakening and improved formability in

magnesium rare earth alloys, Mater. Sci. Technol. 31 (2015) 10–24.
[11] B. Srinivasarao, N.V. Dudamell, M.T. Pérez-Prado, Texture analysis of the effect of non-basal slip systems on the dynamic recrystallisation of the Mg alloy AZ31, Mater. Charact. 75 (2013) 101–107.
[12] D. Guan, W.M. Rainforth, L. Ma, B. Wynne, J. Gao, Twin recrystallisation mechanisms and exceptional contribution to texture evolution during annealing in a magnesium alloy, Acta Mater. 126 (2017) 132–144.
[13] N. Stanford, M.R. Barnett, The origin of “rare earth” texture development in extruded Mg-based alloys and its effect on tensile ductility, Mater. Sci. Eng. A 496 (2008) 399–408.
[14] N. Stanford, D. Atwell, A. Beer, C. Davies, M.R. Barnett, Effect of microalloying with rare-earth elements on the texture of extruded magnesium-based alloys, Scr. Mater. 59 (2008) 772–775.
[15] M. Sanjari, A. Farzadfar, A.S.H. Kabir, H. Utsunomiya, I.-H. Jung, R. Petrov, L. Kestens, S. Yue, Promotion of texture weakening in magnesium by alloying and thermomechanical processing: (I) alloying, J. Mater. Sci. 49 (2014) 1408–1425.
[16] J. Bohlen, M.R. Nürnberg, J.W. Senn, D. Letzig, S.R. Agnew, The texture and anisotropy of magnesium–zinc–rare earth alloy sheets, Acta Mater. 55 (2007) 2101–2112.
[17] L.W.F. Mackenzie, M.O. Pekguleryuz, The recrystallisation and texture of magnesium–zinc–cerium alloys, Scr. Mater. 59 (2008) 665–668.
[18] N. Stanford, D. Atwell, M.R. Barnett, The effect of Gd on the recrystallisation, texture and deformation behaviour of magnesium-based alloys, Acta Mater. 58 (2010) 6773–6783.
[19] J.D. Robson, D.T. Henry, B. Davis, Particle effects on recrystallisation in magnesium–manganese alloys: particle-stimulated nucleation, Acta Mater. 57 (2009) 2739–2747.
[20] I. Basu, T. Al-Samman, Twin recrystallisation mechanisms in magnesium-rare earth alloys, Acta Mater. 96 (2015) 111–132.
[21] P. Hidalgo-Manrique, S.B. Yi, J. Bohlen, D. Letzig, M.T. Pérez-Prado, Effect of Nd additions on extrusion texture development and on slip activity in a Mg-Mn alloy, Metall. Mater. Trans. A 44 (2013) 4819–4829.
[22] Z.R. Zeng, Y.M. Zhu, S.W. Xu, M.Z. Bian, C.H.J. Davies, N. Birbilis, J.F. Nie, Texture evolution during static recrystallisation of cold-rolled magnesium alloys, Acta Mater. 105 (2016) 479–494.
[23] J. Robson, S. Haigh, B. Davis, D. Griffiths, Grain boundary segregation of rare-earth elements in magnesium alloys, Metall. Mater. Trans. A (2015) 1–9.
[24] J. Robson, Effect of rare-earth additions on the texture of wrought magnesium alloys: the role of grain boundary segregation, Metall. Mater. Trans. A 45 (2014) 3205–3212.
[25] I. Basu, T. Al-Samman, Triggering rare earth texture modification in magnesium alloys by addition of zinc and zirconium, Acta Mater. 67 (2014) 116–133.
[26] C. Drouven, I. Basu, T. Al-Samman, S. Korte-Kerzel, Twinning effects in deformed and annealed magnesium–neodymium alloys, Mater. Sci. Eng. A 647 (2015) 91–104.
[27] F.J. Humphreys, M. Hatherly, Recrystallisation and Related Annealing Phenomena, Elsevier Science, 2004.
[28] B.-C. Suh, M.-S. Shim, K.S. Shin, N.J. Kim, Current issues in magnesium sheet alloys: where do we go from here? Scr. Mater. 84–85 (2014) 1–6.
[29] T. Al-Samman, G. Gottstein, Dynamic recrystallisation during high temperature deformation of magnesium, Mater. Sci. Eng. A 490 (2008) 411–420.
[30] A. Levinson, R.K. Mishra, R.D. Doherty, S.R. Kalidindi, Influence of deformation twinning on static annealing of AZ31 Mg alloy, Acta Mater. 61 (2013) 5966–5978.
[31] X. Li, P. Yang, L.N. Wang, L. Meng, F. Cui, Orientational analysis of static recrystallisation at compression twins in a magnesium alloy AZ31, Mater. Sci. Eng. A 517 (2009) 160–169.
[32] K.D. Molodov, T. Al-Samman, D.A. Molodov, G. Gottstein, Mechanisms of exceptional ductility of magnesium single crystal during deformation at room temperature: multiple twinning and dynamic recrystallisation, Acta Mater. 76 (2014) 314–330.
[33] É. Martin, R.K. Mishra, J.J. Jonas, Effect of twinning on recrystallisation textures in deformed magnesium alloy AZ31, Philos. Mag. 91 (2011) 3613–3626.
[34] S. Niknejad, S. Esmaeili, N.Y. Zhou, The role of double twinning on transgranular fracture in magnesium AZ61 in a localized stress field, Acta Mater. 102 (2016) 1–16.
[35] H. El Kadiri, C.D. Barrett, J. Wang, C.N. Tomé, Why are twins profuse in magnesium? Acta Mater. 85 (2015) 354–361.
[36] K.D. Molodov, T. Al-Samman, D.A. Molodov, Profuse slip transmission across twin boundaries in magnesium, Acta Mater. 124 (2017) 397–409.
[37] M. Lentz, A. Behringer, C. Fahrenson, I.J. Beyerlein, W. Reimers, Grain size effects on primary, secondary, and tertiary twin development in Mg-4 wt pct Li (-1 wt pct Al) alloys, Metall. Mater. Trans. A 45 (2014) 4737–4741.
[38] P.A. Beck, P.R. Sperry, Strain induced grain boundary migration in high purity aluminum, J. Appl. Phys. 21 (1950) 150–152.
[39] J.D. Robson, S.J. Haigh, B. Davis, D. Griffiths, Grain boundary segregation of rare-earth elements in magnesium alloys, Metall. Mater. Trans. A 47 (2016) 522–530.
[40] J.P. Hadorn, T.T. Sasaki, T. Nakata, T. Ohkubo, S. Kamado, K. Hono, Solute clustering and grain boundary segregation in extruded dilute Mg–Gd alloys, Scr. Mater. 93 (2014) 28–31.
[41] J. Hadorn, K. Hantzsche, S. Yi, J. Bohlen, D. Letzig, J. Wollmershauser, S. Agnew, Role of solute in the texture modification during hot deformation of Mg-Rare earth alloys, Metall. Mater. Trans. A 43 (2012) 1347–1362.
[42] L.L. Rokhlin, Magnesium Alloys Containing Rare Earth Metals : Structure and Properties, Taylor & Francis, London, 2003.
[43] D. Guan, J. Nutter, J. Sharp, J. Gao, W. Mark Rainforth, Direct observation of precipitation along twin boundaries and dissolution in a magnesium alloy annealing at high temperature, Scr. Mater. 138 (2017) 39–43.
[44] P. Changizian, A. Zarei-Hanzaki, M. Ghambari, A. Imandoust, Flow localization during severe plastic deformation of AZ81 magnesium alloy: micro-shear banding phenomenon, Mater. Sci. Eng. A 582 (2013) 8–14.
[45] M.J. Jones, F.J. Humphreys, Interaction of recrystallisation and precipitation: the effect of Al3Sc on the recrystallisation behaviour of deformed aluminium, Acta Mater. 51 (2003) 2149–2159.
[46] S.A. Farzadfar, É. Martin, M. Sanjari, E. Essadiqi, S. Yue, Texture weakening and static recrystallisation in rolled Mg–2.9Y and Mg–2.9Zn solid solution alloys, J. Mater. Sci. 47 (2012) 5488–5500.
[47] K. Hantzsche, J. Bohlen, J. Wendt, K.U. Kainer, S.B. Yi, D. Letzig, Effect of rare earth additions on microstructure and texture development of magnesium alloy sheets, Scr. Mater. 63 (2010) 725–730.
[48] M. Chatterton, J. Robson, D. Henry, Texture evolution during wire drawing of Mg-RE alloy, in: M. Alderman, M.V. Manuel, N. Hort, N.R. Neelameggham (Eds.), Magnesium Technology 2014, Springer International Publishing, Cham, 2016, pp. 251–256.
[49] N. Stanford, G. Sha, J.H. Xia, S.P. Ringer, M.R. Barnett, Solute segregation and texture modification in an extruded magnesium alloy containing gadolinium, Scr. Mater. 65 (2011) 919–921.
[50] Y.M. Kim, C. Mendis, T. Sasaski, D. Letzig, F. Pyczak, K. Hono, S. Yi, Static recrystallisation behaviour of cold rolled Mg-Zn-Y alloy and role of solute segregation in microstructure evolution, Scr. Mater. 136 (2017) 41–45.
[51] R. Cottam, J. Robson, G. Lorimer, B. Davis, Dynamic recrystallisation of Mg and Mg–Y alloys: crystallographic texture development, Mater. Sci. Eng. A 485 (2008) 375–382.